Boundary-Layer Meteorol
DOI 10.1007/s10546-011-9672-7

ARTICLE

# High-Resolution Fibre-Optic Temperature Sensing: A New Tool to Study the Two-Dimensional Structure of Atmospheric Surface-Layer Flow

**Christoph K. Thomas · Adam M. Kennedy · John S. Selker · Ayla Moretti · Martin H. Schroth · Alexander R. Smoot · Nicholas B. Tufillaro · Matthias J. Zeeman**

Received: 10 June 2011 / Accepted: 31 October 2011


**Abstract** We present a novel approach based on fibre-optic distributed temperature sensing (DTS) to measure the two-dimensional thermal structure of the surface layer at high resolution (0.25 m, ≈0.5 Hz). Air temperature observations obtained from a vertically-oriented fibre-optics array of approximate dimensions 8 m × 8 m and sonic anemometer data from two levels were collected over a short grass field located in the flat bottom of a wide valley with moderate surface heterogeneity. The objectives of the study were to evaluate the potential of the DTS technique to study small-scale processes in the surface layer over a wide range of atmospheric stability, and to analyze the space–time dynamics of transient cold-air pools in the calm boundary layer. The time response and precision of the fibre-based temperatures

C. K. Thomas (✉) · A. M. Kennedy · A. Moretti · A. R. Smoot · N. B. Tufillaro · M. J. Zeeman
College of Oceanic and Atmospheric Sciences, Oregon State University, 104 COAS Admin Bldg., Corvallis, OR 97331, USA
e-mail: chthomas@coas.oregonstate.edu

A. M. Kennedy
e-mail: akennedy@coas.oregonstate.edu

A. Moretti
e-mail: morettia@onid.orst.edu

A. R. Smoot
e-mail: asmoot@coas.oregonstate.edu

N. B. Tufillaro
e-mail: nbt@coas.oregonstate.edu

M. J. Zeeman
e-mail: mjzeeman@coas.oregonstate.edu

J. S. Selker
Department of Biological and Ecological Engineering, Oregon State University, Corvallis, OR 97331, USA
e-mail: john.selker@oregonstate.edu

M. H. Schroth
Institute of Biogeochemistry and Pollutant Dynamics, ETH, Universitätsstr. 16, 8092 Zurich, Switzerland
e-mail: martin.schroth@env.ethz.ch

Published online: 19 November 2011

were adequate to resolve individual sub-metre sized turbulent and non-turbulent structures, of time scales of seconds, in the convective, neutral, and stable surface layer. Meaningful sensible heat fluxes were computed using the eddy-covariance technique when combined with vertical wind observations. We present a framework that determines the optimal environmental conditions for applying the fibre-optics technique in the surface layer and identifies areas for potentially significant improvements of the DTS performance. The top of the transient cold-air pool was highly non-stationary indicating a superposition of perturbations of different time and length scales. Vertical eddy scales in the strongly stratified transient cold-air pool derived from the DTS data agreed well with the buoyancy length scale computed using the vertical velocity variance and the Brunt–Vaisala frequency, while scales for weak stratification disagreed. The high-resolution DTS technique opens a new window into spatially sampling geophysical fluid flows including turbulent energy exchange.

**Keywords** Cold-air pool · Distributed temperature sensing · Fibre optics · Spatial sampling · Stable boundary layer · Taylor's hypothesis · Turbulence

## 1 Introduction

The transfer of sensible heat between the atmosphere and land surface as a component of the surface energy balance is required for the estimation of evapotranspiration in agriculture, dispersion of air-borne pollutants, climate change science, as well as in fundamental research studying the nature of turbulent heat exchange. Temperature is considered an active scalar since it has a dominant effect on the density of an air parcel and thus its buoyancy. It may determine, e.g., whether a contaminant released close to the ground will spread rapidly and become diluted through the entire atmospheric boundary layer, or whether it stays confined to a shallow layer close to the ground as in the case of stably stratified flows. The use of heat as a tracer in geophysical fluid flows has also led to the formulation of similarity theory concepts that are at the core of operational and research-grade weather and climate numerical models to parametrize energy fluxes at spatial scales smaller than the grid size. Similarity theories that relate characteristics of the land surface such as topography and vegetation height to the atmospheric exchange of momentum and heat are posed in terms of length scales. In contrast, most observations used to formulate these concepts have been made in the time domain at a single point in space by invoking the ergodic hypothesis, which states that time and space averages converge under stationary horizontally homogeneous conditions. Time scales are then commonly converted into the space domain by assuming the validity of Taylor's hypothesis stating that temporal gradients are related to spatial gradients through the speed of the mean flow (Taylor 1938). While the validity of these fundamental assumptions has been demonstrated as a rough approximation for many geophysical fluid flows, evidence has mounted that they may be invalid for atmospheric motions that dominate the diffusion and dispersion of energy and matter in the stable boundary layer. Under those conditions, the speed of the mean flow can be smaller than the magnitude of individual perturbations driving the transport. Examples include meandering of the flow (Anfossi et al. 2005), occurrence of density currents (Sun et al. 2002, 2004), sudden wind-direction shifts (Mahrt 2008) and within-canopy flow and heat transport (Thomas 2011). Although some progress has been made by analyzing observations from sensor networks (e.g. Mahrt et al. 2009), the lack of sufficiently dense spatial information has prevented progress on much-needed improvements for existing similarity theory concepts with the goal to reducing the uncertainty of weather, climate, and air pollution model predictions, particularly in physically not well-understood

conditions such as the stable boundary layer. Technological advances have led to the development of distributed temperature sensing (DTS) methods that use fibre-optic cables as sensing elements (Selker et al. 2006a,b; Tyler et al. 2009). This sensor has the potential for spatially dense sampling of environmental processes using temperature as a flow tracer at a relatively low cost. To date, applications have mainly focused on surface hydrology (e.g. Selker et al. 2006a; Westhoff et al. 2007; Tyler et al. 2008) with only few applications in the atmosphere (e.g. Keller et al. 2011; Petrides et al. 2011). These studies have primarily focused on process scales of minutes and metres in a one-dimensional (1-D) sampling framework in streams or vertical profiles in the atmosphere. Recent developments have increased the resolution of the instruments to sub-metre and seconds and now have the potential to satisfy the high demands for sampling the small scales and rapidly changing gradients associated with individual turbulent eddies rather than the time- or space-averaged flow.

The objectives of this first study using high-resolution DTS in the atmosphere are twofold:

- Evaluating the potential of the high-resolution DTS for atmospheric surface-layer applications where eddy sizes are small and the local surface heterogeneity may be important. For this purpose, we compare single-point statistics including time series, spectra, and sensible heat fluxes based on the DTS observations to those collected from closely collocated sonic anemometers (Sects. 3.1, 3.2).
- Analyzing the space–time dynamics of the nocturnal stable boundary layer when micro cold-air pools prevail at the experimental site (Sect. 3.3). These air pools are relevant to human health, vegetation patterns, and road traffic by trapping moisture and pollutants within the lowest few metres in the air above the ground often leading to surface fog and maximum concentrations near the ground surface.

## 2 Experimental Set-Up

Fibre temperature data, $T_f$, were collected from a vertically oriented two-dimensional (2-D) array of approximate dimensions 8 m × 8 m oriented in west (W)–east (E) direction above a grass field on the grounds of an agricultural field research station near Corvallis, OR, USA over the period 30 September until 22 October 2010 (Figs. 1, 2). The bottom of the fibre array

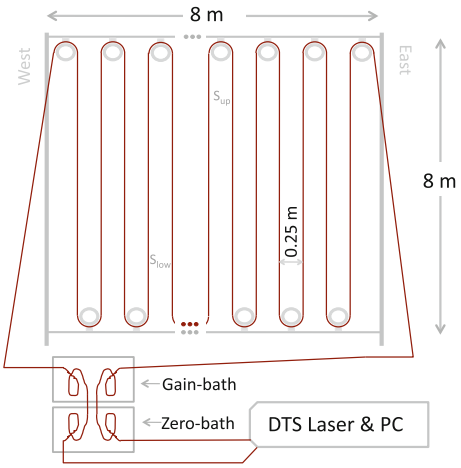


**Fig. 1** Schematic experimental set-up of the two-dimensional fibre-optics array and positions of the sonic anemometers ($S_{low}$, $S_{up}$). Only one fibre strand (*black lines*) is shown for clarity of presentation. Elements are not drawn to scale

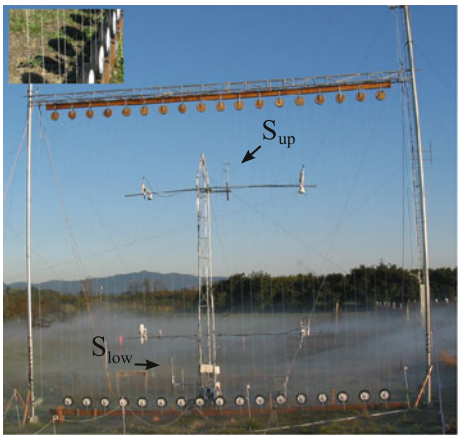


**Fig. 2** Photo of the fibre-optics array showing the position of the upper ($S_{up}$) and lower ($S_{low}$) sonic anemometers used for comparison with the DTS method. The *inset* in the *upper left corner* shows the two parallel fibre strands of *black* and *white colour*, which were spaced at 0.02m in the north–south direction. Also visible are four aspirated thermo-hygrometers and machine-generated fog near the ground, for which analyses are not presented here

was ≈0.5 m offset from the ground surface. Two optical fibre strands of identical composition (tightly buffered, aramid reinforced injection-molded multi-mode fibre with a total diameter of 900 μm, 50 μm glass core and 37 μm glass cladding, terminated with a E2000 connector; AFL Telecommunications LLC, Spartanburg, South Carolina, USA), but different black and white colours were suspended by grooved pulleys keeping the two fibres at a constant separation distance of 0.02 m. The horizontal spacing of the pulleys was equal to twice their diameter of 0.25 m to construct an array with an even spacing between fibre strands. Measurements were made using a DTS instrument (Model Ultima, Silixa, Elstree, Hertfordshire, United Kingdom) reporting $T_f$ averaged over 1 s (time) and 0.125-m increments (space) m along the entire length of the fibre of ≈600 m, yielding ≈2000 individual measurements within the array. The reader is referred to Selker et al. (2006b) and Tyler et al. (2009) for a comprehensive description of the operating principles of range-gaged Raman spectra DTS and a more detailed explanation of technical information described here. During post-processing, recorded $T_f$ data were spatially averaged to a 0.25-m resolution along the fibre to yield a rectangular and evenly spaced matrix with a grid size of 0.25 m in both the vertical and horizontal directions. Both fibres were connected to the instrument in a double-ended configuration, i.e., both ends of each fibre were attached to and used by the DTS instrument to inject light. However, measurements from the same fibre, but different directions, were stored and analyzed separately (as a single-ended measurement) to maximize the temporal resolution. The sampling sequence consisting of four measurements (1: white, W → E; 2: black, W → E; 3: white, E → W; 4: black, E → W) was completed within 5–8 s, and repeated continuously over the course of the experiment. The temporal spacing between individual measurements varied between 1 and 3 s, which led to an effective sampling frequency of ≈0.5 Hz and to non-evenly spaced time series and effects discussed further below. The 1-D sampling framework of $T_f$ along the fibre was converted to the 2-D framework of the array by utilizing the fixed pulley locations that were clearly visible in the temperature traces during daylight hours due to solar heating. The 2-D matrices were then spatially low-pass filtered using a biorthogonal wavelet algorithm (Thomas and Foken 2005) retaining only perturbations corresponding to spatial scales ≥0.5 m in both the vertical and horizontal directions to remove small-scale variability present in the data. The filter, however, was found to have little effect on the statistics presented below and was mainly applied for visual smoothing of the data. For calibration purposes, coiled sections of both fibres several metres in length were routed through two slush water baths of different temperature: the 'zero-bath' was filled with

water-saturated crushed ice keeping its temperature nearly constant, while the 'gain-bath' was allowed to vary its temperature following changes in the ambient air temperature with a dampened amplitude and time lag due its thermal inertia. Calibration bath temperatures were taken independently with reference thermometers (Pt-1000, Model 41342, RM Young Company, Traverse City, Michigan, USA) and recorded every 1 s with an external data logger (Model CR3000, Campbell Scientific Inc., Logan, Utah, USA). During post-processing, each recorded $T_f$ measurement was linearly corrected for offset, gain, and signal loss along the fibre using the known bath temperatures, while the instrument's built-in routines were used to correct for differential attenuation. To evaluate the performance of the DTS system, wind speed, $U$, and sonic air temperature, $T_s$, were sampled independently using two ultrasonic anemometers (Model USA FHN-1, Metek, Elmshorn, Germany) recorded at 10 Hz at two heights, 1.5 and 5.9 m above ground level ($S_{low}$ and $S_{up}$ in Fig. 2), closely collocated with the fibre strands within 0.1-m lateral separation. For the purpose of the comparison, we neglected the small influence of water vapour pressure perturbations on $T_s$ as latent heat fluxes during the observation period were generally very small ($\leq 30\,\mathrm{W\,m^{-2}}$).

## 3 Results and Discussion

The dataset was stratified into four different flow regimes with the intention of evaluating the performance of the fibre-optics technique for typical states of the atmospheric surface layer. The regimes were determined by visually inspecting the hourly time series and sorting them according to the observed light regime and the following characteristics:

- shear: day or night; high wind speeds; mechanically generated turbulent eddies dominate with typical time scales between 5 and 20 s; $1.6\,\mathrm{m\,s^{-1}} \leq U \leq 3.1\,\mathrm{m\,s^{-1}}$, $-0.11 \leq \zeta \leq 0.08$, $-0.02 \leq Ri_b \leq -0.01$.
- convective: day; moderate wind speeds; thermally generated turbulent eddies dominate with time scales $\geq$30 s; $0.7\,\mathrm{m\,s^{-1}} \leq U \leq 1.6\,\mathrm{m\,s^{-1}}$, $-1.60 \leq \zeta \leq -0.14$, $-0.23 \leq Ri_b \leq -0.03$.
- quiescent: sunset, sunrise, night; calm conditions; fine-scale turbulent eddies dominate with time scales $\leq$5 s; $0.4\,\mathrm{m\,s^{-1}} \leq U \leq 1.2\,\mathrm{m\,s^{-1}}$, $-0.4 \leq \zeta \leq 0.3$, $-0.26 \leq Ri_b \leq 0.16$.
- submeso: night; weak winds; non-turbulent structures dominate with time scales of minutes, intermittent turbulence and mixing; $0.3\,\mathrm{m\,s^{-1}} \leq U \leq 0.5\,\mathrm{m\,s^{-1}}$, $0.2 \leq \zeta \leq 0.9$, $1.7 \leq Ri_b \leq 7.7$.

The ranges indicated for the horizontal wind speed, $U$, the Obukhov stability parameter stability $\zeta = zL^{-1}$ with $z$ being the height above ground and $L$ the Obukhov length, represent the 25 and 75% percentiles evaluated from the sonic data at 5.9 m. The bulk Richardson number, $Ri_b$, was evaluated from the difference in sonic temperature between the 5.9 and 1.5 m levels. Examples of time series for the shear and submeso regimes are given in Fig. 3.

### 3.1 Time Response and Precision

A sensor's ability to capture the rapidly changing space–time gradients, characteristic of turbulent flows, is of paramount importance for its successful use in environmental studies, while its accuracy is of secondary interest for the computation of perturbations from the mean state based on the Reynolds decomposition and turbulent fluxes. The time and frequency response of the DTS system was evaluated by extracting the temperature time series of the fibre increments next to the sonic anemometers, linearly interpolating them to 10 Hz to match sampling

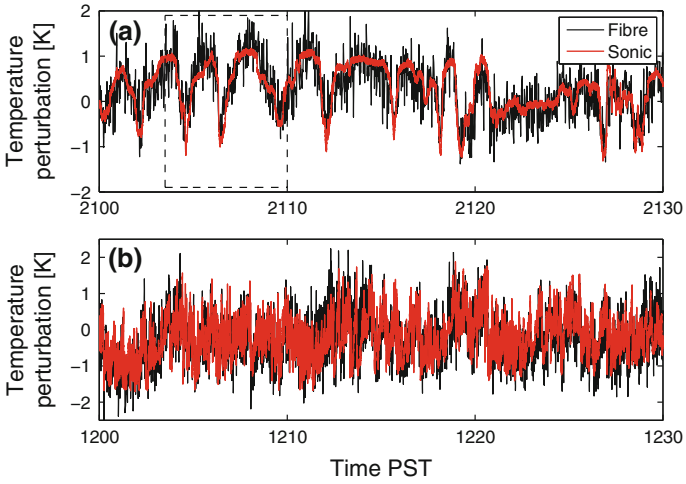


**Fig. 3** Sample time series of fibre and sonic air temperature perturbations observed at a height of 5.9 m for the **a** submeso and **b** shear regimes. The sonic data were sampled at 10 Hz, the fibre at ≈0.5 Hz. Traces were normalized by subtracting the time-averaged hourly temperature. *Dashed box* in **a** indicates period displayed in Fig. 7

frequencies, and computing hourly power spectra by orthogonally decomposing them into the frequency domain using the multi-resolution decomposition algorithm (Howell and Mahrt 1997). The multi-resolution technique decomposes a signal into unweighted averages over increments of dyadic width, which in our case resulted in decomposition modes of 0.1, 0.2, 0.4 s, 0.8, 1.6, 3.2, 6.4, 12.8, 25.6, 51.2, 102.4, 204.8, 409.6, 819.2, and 1638.4 s. We chose the multi-resolution decomposition over other commonly used spectral analysis techniques including the Fourier transform, since it is a local transform and does not make assumptions about the periodicity of the signal, and is insensitive to aliasing. Multi-resolution decomposition spectra obey scaling laws such as, e.g., the $-5/3$ or $-1$ decay of spectral energy in the inertial and production subranges, but typically show a shifted peak density compared to Fourier spectra (Howell and Mahrt 1997). Ensemble-averaged power spectra were then computed using the hourly spectra for the four different flow regimes described above.

In general, the fibre-optics system showed a good agreement in both time response and precision for perturbation time scales $\geq$6.4 s irrespective of the flow regime when compared to the data collected from the sonic anemometers (Fig. 4a,b). An agreement in time response can be identified by a similar shape of the spectral lines, while an agreement in precision is indicated by close agreement in spectral densities. Instrument noise was evident for the quiescent, submeso, and convective regimes for short time scales. For these scales, the variability in $T_f$ is dominated by set-up and instrument artifacts that raise its spectral density above that of the reference instrument and the $2/3$ power scaling law. Note that this power law is equal to the more commonly known $-5/3$ law and differs only due to our choices of the normalization method and abscissa. The time scale of the noise will be discussed in more detail below.

The best agreement was found for the shear and convective flow regimes, when well-developed turbulent eddies dominate the heat exchange. Perturbations smaller than the native sampling time scale of ≈2 s (dashed lines in Fig. 4a,b) cannot be captured by the system and spectral densities shown resulted solely from the linear interpolation of the $T_f$ data. The time response and precision of the fibre-optics system generally showed a better agreement for the upper comparison level at 5.9 m than for the lower height at 1.5 m, which can be explained

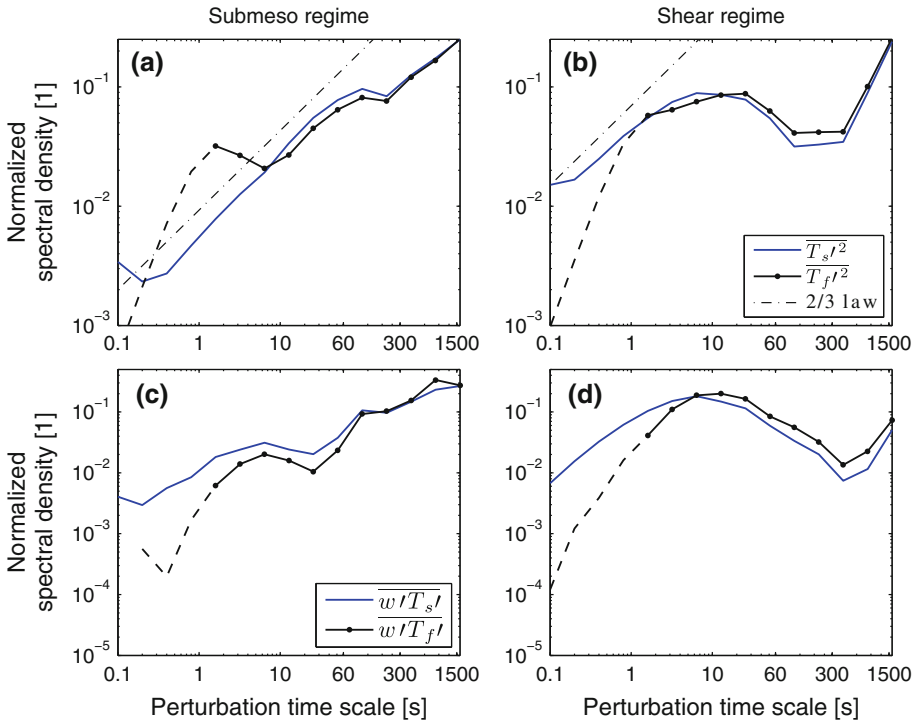


**Fig. 4** Ensemble-averaged **a**, **b** power spectra of the sonic ($T_s$) and fibre optics ($T_f$) air temperatures, and **c**, **d** cospectra of the sensible heat flux computed using the sonic anemometer ($\overline{w'T_s'}$) and the fibre-optics ($\overline{w'T_f'}$) temperatures at 5.9 m for the submeso (**a**, **c**, averaged over 38 h) and shear (**b**, **d**, averaged over 40 h) regimes. *Dashed lines* indicate the time scales resulting from the linear interpolation of the fibre-optics temperature. Also shown is the 2/3 power law for the inertial subrange

by the increasing size of turbulent eddies with increasing distance from the ground. In more general terms, the minimum eddy length scale, $\ell$, that is well resolved by the DTS system has an advection time scale past the fibre-optics cable, $\tau_{\text{eddy}}$, that must be greater than the time response $\tau$ of the DTS system. If for the sake of argument one assumes the validity of Taylor's hypothesis, then

$$\ell = \tau_{\text{eddy}} U > \tau U, \tag{1}$$

where the advection speed is equal the mean horizontal velocity, $U$. The time response of the fibre-optics system, $\tau$, is either limited by the time it takes for the thermal signal of a passing eddy to be registered by the fibre-optics system, $\tau_H$, or equal to the effective time scale of the experimental set-up, $\tau_{\text{setup}}$, whichever is greater (Eq. 2).

$$\tau = \tau_{\text{H}} \text{ with } \tau_{\text{H}} = \tau_{\text{conv}} + \tau_{\text{cond}}; \text{ or } \tau = \tau_{\text{setup}}, \tag{2}$$

where $\tau_{\text{conv}}$ is the convective time scale of the heat transfer between the cable and the air, $\tau_{\text{cond}}$ is the conductive time scale of the radial heat transfer within the cable, and $\tau_{\text{setup}}$ is the time scale associated with the experimental set-up. The convective time scale varies with the boundary-layer conditions in the vicinity of the fibre, which in the case of a perpendicular flow around a cylindrical body can be written as (e.g. Bejan 2004)

$$\tau_{\mathrm{conv}} = \frac{d^2}{\alpha_{\mathrm{a}}} = \frac{d^2\ \rho_{\mathrm{a}}\ c_{\mathrm{p,a}}}{k_{\mathrm{a}}} = \frac{d^2\ \rho_{\mathrm{a}}\ c_{\mathrm{p,a}}\ Nu}{h\ L_{\mathrm{conv}}} = \frac{d\ \rho_{\mathrm{a}}\ c_{\mathrm{p,a}}}{h}, \tag{3}$$

where $d$ is the depth of the boundary layer around the cable [m], $\alpha_a$ the thermal diffusivity of air [m$^2$ s$^{-1}$], $\rho_{\mathrm{a}}$ the air density [kg m$^{-3}$], $c_{\mathrm{p,a}}$ the specific heat of air at constant pressure [J kg$^{-1}$ K$^{-1}$], $k_a$ the thermal conductivity of air [W m$^{-1}$ K$^{-1}$], $h$ the heat transfer coefficient [W m$^{-2}$ K$^{-1}$], $L_{\mathrm{conv}}$ the length of the convection region over the cable [m], and $Nu$ the Nusselt number defined as $Nu = L_{\mathrm{conv}} d^{-1}$.

The conductive time scale is constant for a given fibre diameter and material and is defined as

$$\tau_{\mathrm{cond}} = \frac{r_{\mathrm{cable}}^2}{\alpha_{\mathrm{cable}}}, \tag{4}$$

where $r_{\mathrm{cable}}$ is the radius of the fibre-optics cable [m] and $\alpha_{\mathrm{cable}}$ the thermal diffusivity of the fibre-optics cable [m$^2$ s$^{-1}$]. The time scale of the measurement set-up $\tau_{\mathrm{setup}}$ is equal to the effective time scale of the noise or measurement uncertainty in the fibre temperature observations, and is a function of the DTS instrument, the measurement configuration, and the surface-layer conditions. The main components affecting $\tau_{\mathrm{setup}}$ include, the (i) uncertainty and integration time of counting the inelastically scattered photons by the photodetector inside the DTS instrument, (ii) aforementioned irregular temporal spacing of subsequent measurements, (iii) effects of reading black and white coloured fibre strands experiencing differential heating leading to a temperature increase of the black fibre during daylight hours, which increases the variance at scales twice the sampling resolution (≈4 s) given the sampling sequence of alternating between black and white cables, and (iv) signal-to-noise ratio for small eddies of time scales similar to that of the sampling resolution of $T_{\mathrm{f}}$. Unlike the conductive and convective time scales, $\tau_{\mathrm{setup}}$ cannot be derived analytically. It needs to be estimated empirically using the spectral comparison with the sonic anemometers (Fig. 4) for each flow regime since components (iii) and (iv) depend on the boundary-layer conditions. From the spectral comparison and evaluating Eqs. 3 and 4 one yields $\tau_{\mathrm{conv}} \ll \tau_{\mathrm{cond}} < \tau_{\mathrm{setup}}$ with $\tau_{\mathrm{conv}} \approx 6 \times 10^{-3}$ s, $\tau_{\mathrm{cond}} \approx 1.1$ s, and $\tau_{\mathrm{setup}} \approx 1.6$, 6.4, 12.8, and 3.2 s for the shear, convective, quiescent, and submeso regimes respectively. Note that $\tau_{\mathrm{setup}}$ is instrument-specific and expected to be significantly smaller for future, technically more advanced, sensors. If the convective time scale dominates, one predicts that $\ell > \tau_H\ U \propto U^{1-b}$ by combining Eqs. 1–4, since $h \propto Nu \propto Re^b \propto U^b$ with $b = 0.5$ (King 1914); $Re$ is the Reynolds numbers. However, since $\tau_{\mathrm{conv}} \ll \tau_{\mathrm{cond}}$, the performance of the DTS system decreases almost linearly with increasing horizontal wind speed as the minimum eddy size $\ell$ physically resolved by the sensor increases. On the other hand, the performance of the fibre-optics system is expected to increase with increasing height since $\ell \approx z$ except for very stable conditions and $z$-less scaling. The relationship between horizontal wind speed, observation height, and DTS performance can be used to define an optimal range for the application of DTS in the atmospheric surface layer (Fig. 5). In general, the DTS performs better for lower wind speeds and greater heights. This finding is supported empirically by the spectral analysis and the results presented in the subsequent section. However, we recall that the time scale associated with the experimental set-up $\tau_{\mathrm{setup}}$, also depends on the signal-to-noise ratio. This effect causes a reduction of $\tau_{\mathrm{setup}}$ particularly for stronger flows of the shear regime that are characterized by highly energetic eddies with $\tau_{\mathrm{eddy}} < 6.4$ s, as shown in Fig. 4b. The area between the two lines for $\tau_{\mathrm{setup}}$ in Fig. 5 marked 'A, B' reflects the dependence on the signal-to-noise ratios, and its borders are rather blurred. As a result, the minimum eddy scale physically resolved by the DTS system may be smaller, and thus its performance better, than predicted by the above equations. An advanced DTS instrument and a refined set-up may lead to improvements in

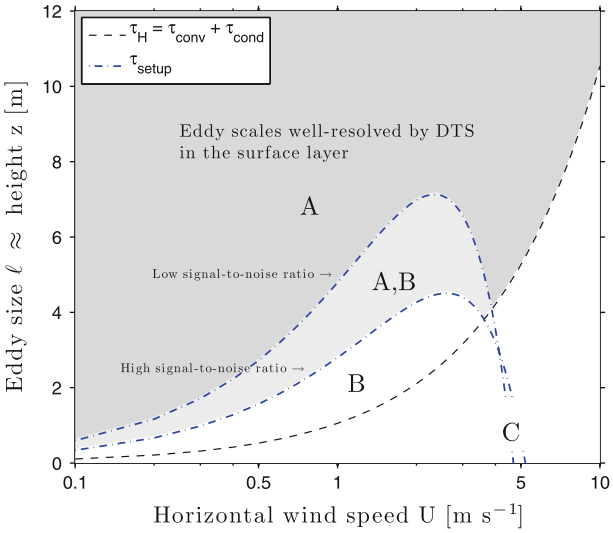


**Fig. 5** Illustration of the potential for applying DTS in the atmospheric surface layer. The *grey-shaded* area (*A*) depicts the ranges of horizontal wind speed and height for which eddy sizes are well resolved by the DTS system deployed in the field experiment. The area is delineated by the limitations arising from the heat transfer from the air to the optical fibre (*black dashed*, $\tau_{conv}$ and $\tau_{cond}$, see Eqs. 3 and 4) and from the experimental set-up (*blue dash-dotted*, $\tau_{setup}$). $\tau_{setup}(U)$ was estimated by linearly regressing the empirically determined values against the mean horizontal wind speeds for different signal-to-noise ratios: low (quiescent and convective flow regimes) and high (shear and submeso flow regimes). Also marked is the potential for improvement of the DTS instrument and refinement of the experimental set-up (*B*), and using fibres of smaller diameter and greater thermal diffusivity (*C*). See Sect. 3.1 for more details

resolved eddy scales particularly for the low and moderate wind speeds $U \leq 4\,\mathrm{m\,s^{-1}}$ (area B), whereas a fibre with smaller diameter and greater thermal diffusivity would increase the performance particularly for speeds $U > 4\,\mathrm{m\,s^{-1}}$ (area C). Note that for observations in area B, the variance is increased, but the covariance and thus fluxes are assumed to be unaffected (see next section). For observations in area C, variances are decreased in comparison with reference instruments.

### 3.2 Sensible Heat Fluxes

We further evaluated the potential of the fibre-optics system for estimating sensible heat fluxes using the eddy-covariance technique, which has found broad application in studies on land-atmosphere interaction and biogeochemical cycles. In addition to a sufficient frequency response and high precision of the measurements, a correct timing of the measured temperature signal is required to produce physically meaningful flux estimates. To compute heat fluxes using the fibre temperatures, $\overline{w'T_f'}$, time series of $T_f$ were extracted for the fibre increments next to the sonic anemometers, linearly interpolated to match sampling frequencies, and then combined with the vertical velocity time series, $w$, recorded from the sonic anemometer to yield their instantaneous cross-product. The hourly-integrated sensible heat flux, $\overline{w'T_f'}$, was then compared to that from the sonic anemometer, $\overline{w'T_s'}$ for the different flow regimes defined above (Fig. 6). Cospectra were computed using the same multi-resolution decomposition algorithm used for the power spectra (Fig. 4c, d).

The cospectral analysis of the sensible heat fluxes generally confirmed the findings reported in the previous section in that the agreement was good for time scales $\geq$6.4 s,

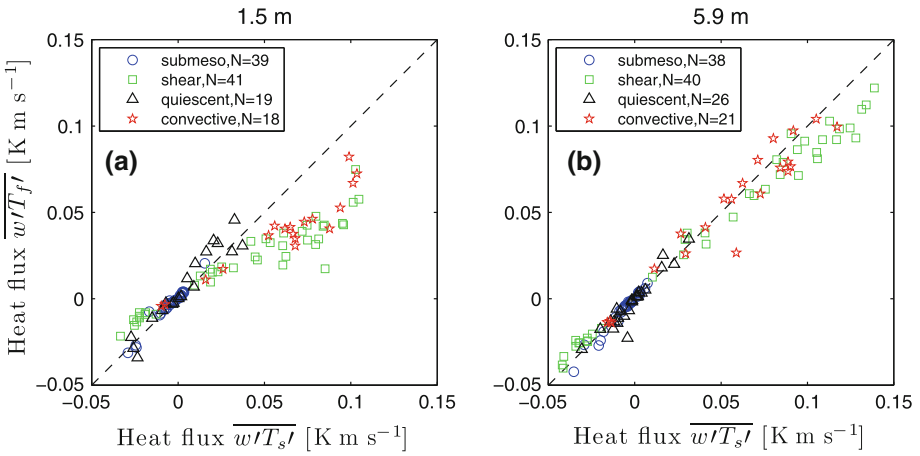


**Fig. 6** Comparison of the hourly-integrated kinematic sensible heat flux using the sonic anemometer temperature ($\overline{w'T_s'}$) and the fibre-optics temperature ($\overline{w'T_f'}$) for the four different flow regimes at both heights. The number ($N$) of hourly flux estimates is given for each regime. The dashed line marks unity. The axes for the kinematic heat fluxes correspond to about $-50$ to 150 W m$^{-2}$ in energetic units

but showed a systematic underestimation for shorter scales. However, the flux transported on these time scales is small and therefore did not lead to a significant underestimation of the magnitude of the hourly-integrated flux, at least for the upper comparison height (Fig. 6). Note that the range of increased variance, which was evident in the power spectra and associated with the instrument noise and experimental set-up, was absent in the cospectra. This artificial part of the signal is uncorrelated with the vertical wind and therefore does not contribute to the covariance. A systematic underestimation of the fibre optics hourly-integrated sensible heat flux was observed during the shear regime case for the upper comparison level, as well as for the convective and shear regimes at the lower level (Fig. 6). Again, these discrepancies can be attributed to the small size of the heat-transporting eddies closer to the ground and the rapid passage of larger eddies for the stronger flows of the shear regime that are insufficiently captured by the DTS system due to its limited time response (compare Fig. 5). Heat fluxes generally agreed well for periods characterized by stable, weak wind regimes when submeso motions dominate, which underlines the strength of DTS technology to observing atmospheric flows under these physically poorly understood conditions. For flux computations utilizing the perturbations from the time-averaged signals of air temperature and vertical velocity, the differential solar heating of both the white and black coloured cables during daylight hours were negligible, despite its magnitude of several K. The differential heating and the energy balance of the white and black fibre optic cables will be the focus of a forthcoming manuscript.

### 3.3 Transient Cold-Air Pool Dynamics

We used the fibre-optics temperatures to visualize and analyze the stable boundary flow by detecting the dynamics of cold air near the ground surface for the submeso flow regime ($N = 38$ hourly intervals). Temperature is an ideal flow tracer in the stable boundary layers because of its distinct thermal signature, which facilitates the detection of structure. The cold-air pool discussed here is different to those typically reported for valleys (e.g. Whiteman et al. 2001; Zhong et al. 2001; Whiteman and Zhong 2008; Fritts et al. 2010; Mahrt et al.

2010; Smith et al. 2010, and references therein). The depth of the valley-scale cold pools can amount to several tens to hundreds of metres and is promoted by sheltering of the surrounding ridges, drainage currents, and radiative cooling. We therefore chose the terminology 'transient cold-air pool' to distinguish it from valley-scale cold-air pools. We further assume that the dynamics discussed below are characteristic of any stable boundary-layer flow over flat terrain. Shallow depressions of vertical scales of less than 1 m on horizontal scales of tens to hundreds of metres similar to that present at the site are very common in landscapes that otherwise lack significant topographical changes. The site is located in the flat bottom lands of the Willamette Valley and significant elevational uprise occurs only at a distance of approximately 6 km to the north-west of the field site. However, the observed vertical temperature differences for the generally shallow transient cold-air pool analyzed here are of similar magnitude as those reported for the much deeper valley inversions and can amount to several K, reaching a maximum of ≈7 K during the observational period. Both valley-scale and transient cold-air pools have practical significance for air quality and traffic as they are often characterized by fog and can trap contaminants, other gases, and particulate matter close to the ground. Additionally, the occurrence of strong and shallow temperature inversions characteristic for both types of cold-air pools leads to significantly steeper local lapse rates, which aggravates the forecast of meaningful local near-surface temperatures from regional models (e.g. Sheridan et al. 2010; Smith et al. 2010).

The upper boundary of the transient cold-air pool, $z_{cp}$, was defined as the height above ground corresponding to the maximum temperature gradient $\partial T_f \partial z^{-1}$ detected in each column of the 2-D array as a function of time, as opposed to a constant isotherm. From this definition it follows that the sampled dynamics of $z_{cp}$ do not necessarily reflect individual structures particularly in the vertical. The dynamics rather represent an estimate of the vertical extent adjacent to the ground over which energy and matter may be transported or mixed. Note that this analysis aims at demonstrating the utility of high-resolution spatially-distributed temperature information to reveal the small-scale structure of the stable boundary-layer flow rather than providing a comprehensive discussion of the transient cold-air pool dynamics.

The height of the cold-air pool was found to be highly variable in both space and time (Fig. 7). Two types of motions were evident: individual structures with horizontal scales of 1.5–2 m were adequately resolved by the array and their passage through the fibre optics was clearly visible (e.g. $t_2, t_3$ in Fig. 7). The other type consisted of motions with horizontal scales exceeding the dimensions of the array, which showed up as an elevated $z_{cp}$ over the entire width of the sampling domain ($t_1$, $t_4$ in Fig. 7). The former type of motion is likely to be turbulent, while the latter may be categorized as submeso because of the much greater spatial and temporal scales. The instantaneous vertical profiles $T_f(z)$ for $t_1$ and $t_4$ also showed an elevated top of transient cold-air pool during the passage of structures. In contrast, profiles taken at $t_2$ and $t_3$ are commonly observed in the stable boundary layer where $z_{cp}$ is located near the ground (Fig. 8a). We found that the superposition of both types of motions was more common than the occurrence of isolated events of either type, which suggests that multiple internal or external forcing mechanisms act on the transient cold-air pool simultaneously. The non-stationarity of the top of the transient cold-air pool creates an unsharp boundary to the warmer overlying air, which was also noted by Mahrt et al. (2010) analyzing the dynamics between downslope drainage flows and the accumulation of cold air in a shallow valley. A spectral analysis of the horizontal scales of the temperature field $T_f$ for various heights (not shown here) did not yield any preferred length scales for the submeso regime, but was indicative of a steady decline of energy from the smallest eddy scale well resolved by the fibre-optics system (≈0.5 m, compare Fig. 5) to the largest scales (8.25 m) independent of height above ground. Contrary to our findings, Belusic and Mahrt (2008) found a preferred

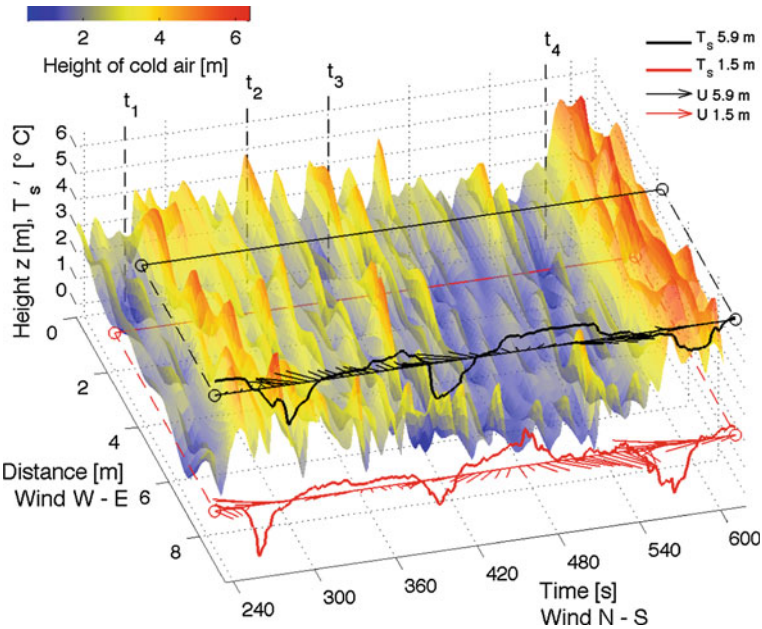


**Fig. 7** Example of the space–time dynamics of the transient cold-air pool in the nocturnal stable boundary layer detected in the 2-D fibre-optics array for the interval indicated by the dashed box in Fig. 3a. *Colours* correspond to the height of the surface representing the maximum vertical temperature gradient. Also shown are the time series of sonic temperature perturbations ($T_s$) and horizontal wind speed and direction ($U$) recorded at two heights, which were laterally displaced for clarity of presentation. Fibre temperatures were collected at ≈0.5 Hz in an evenly spaced grid of resolution 0.25 m (see Sect. 2 for details). The data shown in this graph were low-pass filtered retaining perturbations ≥1.0 m to enhance presentation, but analyses were performed on the data in the aforementioned spatial and temporal resolution

scale for horizontal coherence of the flow in similar conditions for the weak-wind stable boundary layer, but at scales of kilometres far exceeding those of our domain. The presence of both types of motions was independently confirmed by the point observations of sonic temperature showing large negative excursions when the height of the transient cold-air pool was elevated (see $T_s$ traces in Fig. 7).

The time-averaged ensemble statistics of the transient cold-air pool height $z_{cp}$ showed a maximum for $z \leq 2$ m and a secondary peak close to the upper boundary at $z \geq 6$ m of the fibre-optics array (Fig. 8b). This finding suggests that the cold air was generally very shallow constraining the mixing volume to the lowest few metres. Note that observations from the lowest and uppermost 0.6 m of the array were not included in the determination of $z_{cp}$ to avoid possible artifacts resulting from the fibre sections that were in direct contact with or in close proximity to the pulleys. The vertical structure of the boundary layer inferred from $z_{cp}$ was corroborated by the velocity observations from the sonic anemometers, which happened to be installed within and above the mean transient cold pool (black circle and red triangle in Fig. 8a). Perturbation time scales within the transient cold-air pool were much smaller with a peak at ≈1 min, while there was no preferred time scale for the flow aloft showing a steady increase with increasing time scale (Fig. 8c). The time-averaged horizontal wind speeds were generally weak with a peak in the skewed probability density distribution at 0.5 and 0.2 m s$^{-1}$ at 5.9 and 1.5 m, respectively, albeit large scatter between individual intervals particularly at the upper level. The wind directions were highly variable at both levels, often

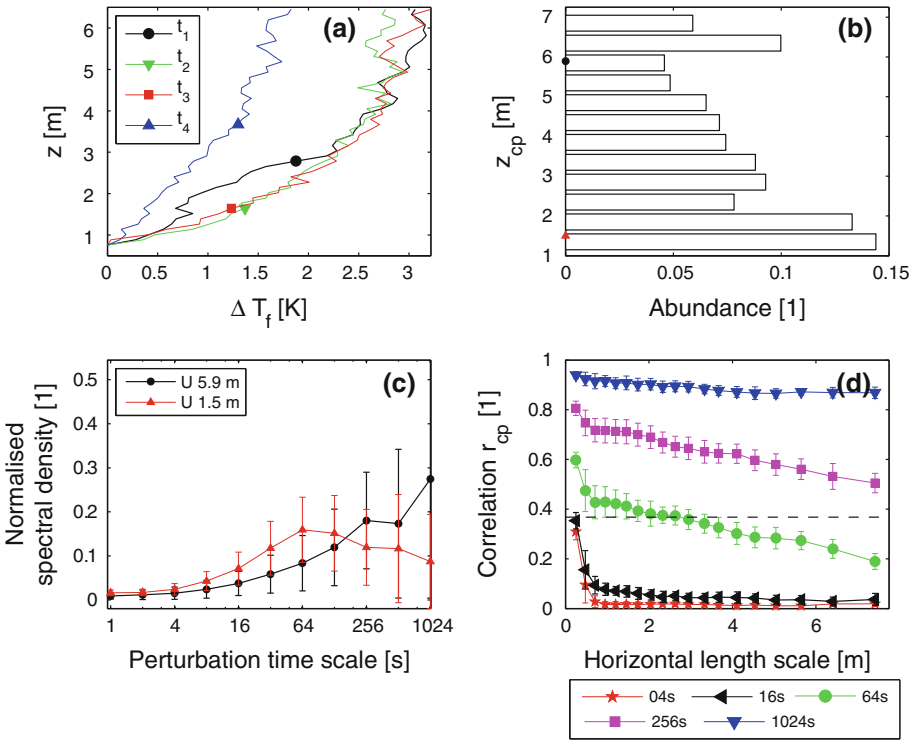


**Fig. 8** Statistics of the transient cold-air pool sampled with the fibre-optics array and sonic anemometers for the submeso regime ($N = 38$ hourly intervals): **a** Instantaneous horizontally averaged profiles of fibre-optics temperature $\Delta T_f$ as a function of height, $z$, for times $t_1$ to $t_4$ indicated in Fig. 7; the position of the marker indicates the detected height of the transient cold-air pool; profiles were normalized by subtracting the bottom temperature to improve the display; **b** *Histogram* of the transient cold-air pool height, $z_{cp}$, horizontally-averaged over the 2-D fibre array; markers indicate the height of the velocity observations used in (**c**); **c** horizontal wind velocity spectra at two heights; individual spectra were normalized by their variance; **d** Time-dependent two-point correlation coefficient of $z_{cp}$ as a function of horizontal scale (separation distance) for various multi-resolution time scales (see Sect. 3.1 for details); the *dashed line* indicates a reduction of the correlation below $e^{-1}$

indicating strong directional shear up to 180° between the two heights. This result underlines the complications when estimating the spatial scales of structures solely based on the traditional 1-D vertical profile or single-point measurement geometry in combination with Taylor's hypothesis (e.g. Thorpe 1977; Smedman et al. 1995; Sorbjan and Balsley 2008).

As the utility of the fibre optics over traditional techniques lies in its ability to provide spatially-distributed observations over time, we calculated the time-dependent two-point correlation coefficient between $z_{cp}$ of all columns for the different multi-resolution decomposition time scales as a measure of the time-space ratio (Fig. 8d). It must be noted that the range of scales covered in the time and space domains was not symmetric due to the limited dimensions of the fibre-optics array compared to the long sampling period. If one assumes the validity of Taylor's hypothesis in these conditions for the sake of estimating this ratio, the time scales equivalent to the resolved spatial scales equate to 16 and 40 s within and above the transient cold-air pool, respectively, as inferred by dividing the horizontal dimension of the array by the mean horizontal velocities for this regime. Because of this asymmetry, we did not

proceed to construct a space–time diagram (as shown in e.g. Belusic and Mahrt 2008; Mahrt et al. 2009; Thomas 2011). The structure of the transient cold-air pool on time scales >1 min generally showed little sensitivity to the horizontal scale by maintaining a high correlation over the entire width of the fibre-optics array, while the shorter-lived structures had generally smaller horizontal length scales as indicated by correlations that rapidly approach zero. In order to enable analysis of the vertical length scales, the time-dependent perturbations were derived by subtracting the time-averaged hourly mean profile from the instantaneous profiles prior to the multi-resolution decomposition. The vertical length scales inferred from the spatial $T_f$ data were found to be insensitive to the vertical temperature gradient. Thermal structures of vertical length scales ≈0.5 m dominated during periods of both weak and strong stratification with mean gradients of ≈0.05 K m$^{-1}$ and ≈0.5 K m$^{-1}$ respectively. Note that motions on scales ≥0.5 m are well resolved by the fibre-optics system in these weak wind conditions. A commonly used limiting vertical length scale in the stable boundary layer is the buoyancy scale $L_B = \sigma_w N_{BV}^{-1}$, with $\sigma_w$ being the square root of the vertical velocity variance and $N_{BV}$ being the Brunt-Vaisala frequency calculated here using the vertical temperature difference between the two sonic anemometer levels. $L_B$ is thought to represent the mean vertical distance a fluid particle can travel before all its vertical fluctuation energy is converted into potential energy (Brost and Wyngaard 1978). For our data, $L_B = 1.8 \pm 0.8$ m in the case of weak gradients, and $L_B = 0.4 \pm 0.1$ m in the case of strong thermal stratification. Note that the shifts in $z_{cp}$ were much larger than $L_B$ in the majority of cases. Estimates of $L_B$ therefore disagree with vertical length scales directly derived from the fibre temperatures for weak stratification, which may suggest that motions contributing to $\sigma_w$ are generated by mechanisms different from those controlling $\partial T_f \partial z^{-1}$ in the absence of significant stratification, at least at this site. The dissimilarity in driving mechanisms between the flow and the temperature field was also observed for observations from a horizontal network located in the sub-canopy of a forest (Thomas 2011), which was only weakly or neutrally stratified.

## 4 Conclusions

We arrive at the following conclusions with regard to the two objectives of this study:

- The fibre-optics system provided an adequate time response, precision, and timing of the measurements to satisfy the demands for sampling individual short-lived and small-scale thermal structures in atmospheric flows for a broad range of conditions. The presented time response and uncertainty analysis also provides a framework for potentially significant improvements in the performance of fibre optic systems for surface-layer applications in the future. The solar heating of the fibre optic cables during sunlight hours had a minor impact on methods concerned with temperature perturbations rather than accuracy of the observations. The computation of sensible heat fluxes using the eddy-covariance technique is possible when combined with vertical velocity data. An additional, purely technical, constraint is posed by the DTS instrument, which currently allows only for a maximum fibre length of ≈2.5 km to be sampled at 0.25-m resolution, yielding roughly 10,000 individual measurements to be distributed in space.
- The analysis of the transient cold-air pool based on the 2-D distributed temperature revealed a superposition of different types of motions of varying time and length scales. The top of the transient cold-air pool is highly non-stationary as it is constantly modified by these perturbations, which may have significant impacts on the diffusion and dispersion of contaminants released and trapped in air near the surface. The length scales of

the shorter, turbulent motions can directly be estimated from the fibre-optics temperature fields, while the domain size in our study was insufficient to allow for direct estimates of length scales for the longer, submeso-scale motions. Future applications of the high-resolution fibre optics DTS technique will need to extend the size of the sampling domain in order to resolve a larger range of horizontal scales in the surface layer. Such experiments would also remedy the asymmetry in observations between space and time domains. The mismatch in vertical scales computed directly from the 2-D temperature fields and those from commonly used parametrizations for the stable boundary layer may indicate that different forcing mechanisms act on the wind and temperature fields, particularly for weakly stratified flows.

The availability of a method suitable to spatially sample fast evolving flows at a high temporal resolution has a broad potential for applications in the environmental sciences. Examples of applications included ecological studies using cold-air drainage to infer ecosystem metabolism (e.g. Pypker et al. 2007), the impact of topography on regional air-flow patterns and valley cold-air pools (e.g. Whiteman et al. 2001; Lundquist et al. 2008; Smith et al. 2010), studies on canopy flow and heat transport (e.g. Bergström and Högström 1989), and direct means to experimentally evaluate large-eddy simulation in the atmospheric boundary layer (e.g. Shaw and Schumann 1992; Bohrer et al. 2009).

**Acknowledgements** This research was funded by the Army Research Office, contracts W911NF-10-1-0361 and W911NF-09-1-0271, and the National Science Foundation, awards AGS 0955444 and 0529223. The fibre-optics instrument was provided by the Center for Transformative Environmental Monitoring Programs (CTEMPS) funded by the National Science Foundation, award EAR 0930061. MHS gratefully acknowledges J. Zeyer and the ETH Zuerich for supporting his sabbatical leave at OSU in autumn 2010. MJZ acknowledges support from the Swiss National Science Foundation Grant PBEZP2-127819. We thank Larry Mahrt and Elie Bou-Zeid for helpful discussions and Evan DeBlander for assisting in the field experiment.

## References

Anfossi D, Oettl D, Degrazia G, Goulart A (2005) An analysis of sonic anemometer observations in low wind speed conditions. Boundary-Layer Meteorol 114(1):179–203

Bejan A (2004) Convection heat transfer, 3rd edn. Wiley, Hoboken, 694 pp

Belusic D, Mahrt L (2008) Estimation of length scales from mesoscale networks. Tellus Ser A Dyn Meteorol Oceanogr 60(4):706–715. doi:10.1111/j.1600-0870.2008.00328.x

Bergström H, Högström U (1989) Turbulent exchange above a pine forest. II. Organized structures. Boundary-Layer Meteorol 49:231–263

Bohrer G, Katul GG, Walko RL, Avissar R (2009) Exploring the effects of microscale structural heterogeneity of forest canopies using large-eddy simulations. Boundary-Layer Meteorol 132(3): 351–382. doi:10.1007/s10546-009-9404-4

Brost RA, Wyngaard JC (1978) Model study of stably stratified planetary boundary-layer. J Atmos Sci 35(8):1427–1440

Fritts DC, Goldstein D, Lund T (2010) High-resolution numerical studies of stable boundary layer flows in a closed basin: evolution of steady and oscillatory flows in an axisymmetric Arizona Meteor Crater. J Geophys Res Atmos 115. doi:10.1029/2009jd013359

Howell JF, Mahrt L (1997) Multiresolution flux decomposition. Boundary-Layer Meteorol 83:117–137

Keller CA, Huwald H, Vollmer MK, Wenger A, Hill M, Parlange MB, Reimann S (2011) Fiber optic distributed temperature sensing for the determination of the nocturnal atmospheric boundary layer height. Atmos Meas Tech 4(2):143–149. doi:10.5194/amt-4-143-2011

King L (1914) On the convection of heat from small cylinders in a stream of fluid: determination of the convection constants of small platinum wires, with applications to hot-wire anemometry. Philos Trans Roy Soc Lond Ser A 214:373–432

Lundquist JD, Pepin N, Rochford C (2008) Automated algorithm for mapping regions of cold-air pooling in complex terrain. J Geophys Res-Atmos 113, doi:10.1029/2008jd009879

Mahrt L (2008) Mesoscale wind direction shifts in the stable boundary-layer. Tellus A 60(4):700–705. doi:10.1111/j.1600-0870.2008.00324.x

Mahrt L, Thomas C, Prueger J (2009) Space–time structure of mesoscale modes in the stable boundary layer. Q J Roy Meteorol Soc 135:67–75

Mahrt L, Richardson S, Seaman N, Stauffer D (2010) Non-stationary drainage flows and motions in the cold pool. Tellus Ser A Dyn Meteorol Oceanogr 62(5):698–705. doi:10.1111/j.1600-0870.2010.00473.x

Petrides A, Huff J, Arik A, Van de Giesen N, Kennedy A, Thomas C, Selker JS (2011) Shade estimation over streams using distributed temperature sensing. Water Resour Res 47:W07,601. doi:10.1029/2010WR009482

Pypker TG, Unsworth MH, Lamb B, Allwine E, Edburg S, Sulzman E, Mix AC, Bond BJ (2007) Cold air drainage in a forested valley: Investigating the feasibility of monitoring ecosystem metabolism. Agric For Meteorol 145(3–4):149–166. doi:10.1016/j.agrfomret.2007.04.016

Selker J, van de Giesen N, Westhoff M, Luxemburg W, Parlange MB (2006a) Fiber optics opens window on stream dynamics. Geophys Res Lett 33(24). doi:10.1029/2006gl027979

Selker JS, Thevenaz L, Huwald H, Mallet A, Luxemburg W, de Giesen NV, Stejskal M, Zeman J, Westhoff M, Parlange MB (2006b) Distributed fiber-optic temperature sensing for hydrologic systems. Water Resourc Res 42(12). doi:10.1029/2006wr005326

Shaw RH, Schumann U (1992) Large-eddy simulation of turbulent-flow above and within a forest. Boundary-Layer Meteorol 61(1–2):47–64

Sheridan P, Smith S, Brown A, Vosper S (2010) A simple height-based correction for temperature downscaling in complex terrain. Meteorol Appl 17(3):329–339. doi:10.1002/met.177

Smedman AS, Bergstrom H, Hogstrom U (1995) Spectra, variances and length scales in a marine stable boundary layer dominated by a low level jet. Boundary-Layer Meteorol 76(3):211–232

Smith SA, Brown AR, Vosper SB, Murkin PA, Veal AT (2010) Observations and simulations of cold air pooling in valleys. Boundary-Layer Meteorol 134(1):85–108. doi:10.1007/s10546-009-9436-9

Sorbjan Z, Balsley BB (2008) Microstructure of turbulence in the stably stratified boundary layer. Boundary-Layer Meteorol 129(2):191–210. doi:10.1007/s10546-008-9310-1

Sun JL, Burns SP, Lenschow DH, Banta R, Newsom R, Coulter R, Frasier S, Ince T, Nappo C, Cuxart J, Blumen W, Lee X, Hu XZ (2002) Intermittent turbulence associated with a density current passage in the stable boundary layer. Boundary-Layer Meteorol 105(2):199–219

Sun JL, Lenschow DH, Burns SP, Banta RM, Newsom RK, Coulter R, Frasier S, Ince T, Nappo C, Balsley BB, Jensen M, Mahrt L, Miller D, Skelly B (2004) Atmospheric disturbances that generate intermittent turbulence in nocturnal boundary layers. Boundary-Layer Meteorol 110(2):255–279

Taylor G (1938) The spectrum of turbulence. Proc R Soc Lond A 164:476–490. doi:10.1098/rspa.1938.0032

Thomas C (2011) Variability of subcanopy flow, temperature, and horizontal advection in moderately complex terrain. Boundary-Layer Meteorol 139:61–81. doi:10.1007/s10546-010-9578-9

Thomas C, Foken T (2005) Detection of long-term coherent exchange over spruce forest using wavelet analysis. Theor Appl Climatol 80:91–104

Thorpe SA (1977) Turbulence and mixing in a Scottish loch. Philos Trans Roy Soc Lond A 286(1334):125–181

Tyler SW, Burak SA, McNamara JP, Lamontagne A, Selker JS, Dozier J (2008) Spatially distributed temperatures at the base of two mountain snowpacks measured with fiber-optic sensors. J Glaciol 54(187):673–679

Tyler SW, Selker JS, Hausner MB, Hatch CE, Torgersen T, Thodal CE, Schladow SG (2009) Environmental temperature sensing using raman spectra DTS fiber-optic methods. Water Resour Res 45:W00D23 doi:10.1029/2008wr007052

Westhoff MC, Savenije HHG, Luxemburg WMJ, Stelling GS, van de Giesen NC, Selker JS, Pfister L, Uhlenbrook S (2007) A distributed stream temperature model using high resolution temperature observations. Hydrol Earth Syst Sci 11(4):1469–1480

Whiteman CD, Zhong SY (2008) Downslope flows on a low-angle slope and their interactions with valley inversions. Part I: Observations. J Appl Meteorol Climatol 47(7):2023–2038. doi:10.1175/2007jamc1669.1

Whiteman CD, Zhong S, Shaw WJ, Hubbe JM, Bian X, Mittelstadt J (2001) Cold pools in the Columbia basin. Wea Forecast 16(4):432–447

Zhong SY, Whiteman CD, Bian XD, Shaw WJ, Hubbe JM (2001) Meterological processes affecting the evolution of a wintertime cold air pool in the Columbia basin. Mon Weather Rev 129(10):2600–2613